How to cite: Angew. Chem. Int. Ed. 2024, e202401818
doi.org/10.1002/anie.202401818

Mg Dual-ion Batteries

Unlocking Four-electron Conversion in Tellurium Cathodes for Advanced Magnesium-based Dual-ion Batteries

Ahiud Morag[+], Xingyuan Chu[+], Maciej Marczewski, Jonas Kunigkeit, Christof Neumann, Davood Sabaghi, Grażyna Zofia Żukowska, Jingwei Du, Xiaodong Li, Andrey Turchanin, Eike Brunner, Xinliang Feng, and Minghao Yu**

Abstract: Magnesium (Mg) batteries hold promise as a large-scale energy storage solution, but their progress has been hindered by the lack of high-performance cathodes. Here, we address this challenge by unlocking the reversible four-electron Te^0/Te^{4+} conversion in elemental Te, enabling the demonstration of superior Mg//Te dual-ion batteries. Specifically, the classic magnesium aluminum chloride complex (MACC) electrolyte is tailored by introducing Mg bis(trifluoromethanesulfonyl)imide ($Mg(TFSI)_2$), which initiates the Te^0/Te^{4+} conversion with two distinct charge-storage steps. Te cathode undergoes $Te/TeCl_4$ conversion involving Cl^- as charge carriers, during which a tellurium subchloride phase is presented as an intermediate. Significantly, the Te cathode achieves a high specific capacity of 543 $mAh\,g_{Te}^{-1}$ and an outstanding energy density of 850 $Wh\,kg_{Te}^{-1}$, outperforming most of the previously reported cathodes. Our electrolyte analysis indicates that the addition of $Mg(TFSI)_2$ reduces the overall ion-molecule interaction and mitigates the strength of ion-solvent aggregation within the MACC electrolyte, which implies the facilized Cl^- dissociation from the electrolyte. Besides, $Mg(TFSI)_2$ is verified as an essential buffer to mitigate the corrosion and passivation of Mg anodes caused by the consumption of the electrolyte $MgCl_2$ in Mg//Te dual-ion cells. These findings provide crucial insights into the development of advanced Mg-based dual-ion batteries.

Introduction

The rapidly expanding battery market, covering portable electronics, electric mobility, and stationary energy storage, underscores the need for next-generation batteries that offer a blend of safety, affordability, durability, and high energy density.[1–3] Among diverse emerging alternatives, rechargeable magnesium (Mg) batteries stand out owing to the utilization of resource-abundant Mg metal anodes, which feature a high specific capacity (2,205 $mAh\,g^{-1}$ and 3,832 $mAh\,cm^{-3}$), low stripping/plating potential (−2.37 V vs. standard hydrogen electrode (SHE)), and absence of dendrite formation.[4–6] While notable progress has been achieved in formulating ethereal electrolytes that facilitate facile Mg stripping/plating,[4,7,8] the advancement of Mg batteries is still hampered by the lack of high-performance cathodes. For instance, intercalation-type cathode materials, exemplified by Chevrel-phase Mo_6S_8 (110 $mAh\,g^{-1}$, 1.1 V vs. Mg)[9–11] and Ti_2S_4 (200 $mAh\,g^{-1}$, 1.2 V vs. Mg),[12] typically exhibit insufficient capacity and operating voltage. Conversion-type cathodes offer much higher specific capacities in comparison with intercalation-type cathodes, such as CoS (360 $mAh\,g^{-1}$, 0.9 V vs. Mg),[13] CuS (440 $mAh\,g^{-1}$, 1.2 V vs. Mg),[14] and S (1081 $mAh\,g^{-1}$, 1.1 V vs. Mg).[15,16] However, conversion-type cathodes often suffer from sluggish reaction kinetics and significant charge/discharge polarization at even a low current density. Besides, emerging coordination-type organic compounds with decent specific capacities present potential use as Mg battery cathodes, such as polyanthraquinonylsulfide (PAQS, 149 $mAh\,g^{-1}$, 1.3 V vs. Mg),[17] polyanthraquinone (P14AQ, 194 $mAh\,g^{-1}$, 1.3 V vs. Mg),[18] and

[*] Dr. A. Morag,[+] X. Chu,[+] D. Sabaghi, J. Du, Dr. X. Li, Prof. X. Feng, Dr. M. Yu
Center for Advancing Electronics Dresden (cfaed) & Faculty of Chemistry and Food Chemistry, Technische Universität Dresden
Mommsenstrasse 4, 01069 Dresden, Germany
E-mail: xinliang.feng@tu-dresden.de
minghao.yu@tu-dresden.de

Dr. A. Morag,[+] Dr. X. Li, Prof. X. Feng
Department of Synthetic Materials and Functional Devices, Max-Planck Institute of Microstructure Physics
06120 Halle, Germany

Dr. M. Marczewski, Dr. G. Z. Żukowska
Faculty of Chemistry, Warsaw University of Technology
Ul. Noakowskiego 3, 00-664 Warsaw, Poland

J. Kunigkeit, Prof. E. Brunner
Chair of Bioanalytical Chemistry, Technische Universität Dresden
01062 Dresden, Germany

Dr. C. Neumann, Prof. A. Turchanin
Institute of Physical Chemistry and Center for Energy and Environmental Chemistry Jena (CEEC Jena), Friedrich Schiller University Jena
Lessingstrasse 10, 07743 Jena, Germany

[+] These authors contributed equally

pyrene-4,5,9,10-tetraone (PTO, 315 mAh g^{-1}, 2.1 V vs. Mg).[4] Nevertheless, owing to their low conductivity, a large content of non-active conducting agents is normally required for the electrode preparation to achieve adequate rate performance, which remains a severe issue limiting the practical application of organic cathodes. Overall, the primary reason for the unsatisfactory performance of previously reported cathodes lies in the divalent Mg^{2+} charge carriers with a giant charge density (120 C mm^{-3}), over double that of Li^+ (54 C mm^{-3}).[19] This high charge density further results in strong interactions between Mg^{2+} and its surroundings, including binding with electrolyte anions/solvent molecules and repulsive forces with the cathode host.[20–22] Consequently, these intricate interactions pose considerable kinetics challenges in cathode electrochemistries, such as large energy barriers requested for Mg^{2+} desolvation/dissociation at the cathode/electrolyte interface and sluggish solid-state Mg^{2+} diffusion within the cathode host.

A promising approach to bypassing the problematic issues of Mg^{2+} charge carriers is to utilize anions in the electrolyte as the cathode charge carriers, constructing Mg batteries based on the dual-ion battery configuration.[23] The dual-ion battery concept has been successfully applied to other multivalent metal batteries, employing either multi-atom anions (such as hexafluorophosphate, bis(trifluoromethanesulfonyl) imide, bis(fluorosulfonyl)imide, and tetrachloroaluminate anions) or halogen anions for cathode electrochemical reactions.[24–27] Typically, these anions show much less charge density than multivalent cations, enabling desirable cathode reaction kinetics. A representative example that has been implemented in multivalent Zn, Ca, and Al batteries is the graphite cathode, which enables high-rate and reversible intercalation of various multi-atom anions.[24,27,28] However, the anion-intercalation electrochemistry of graphite requires a high operating potential (up to 2.1 V vs. SHE), which is incompatible with the anodic stability (less than 1.2 V vs. SHE) of typical ethereal electrolytes used in Mg batteries. Several p-type redox organic compounds, such as phenazine,[29] polytriphenylamine (PTPAn),[23,27] and organosulfur,[30] are also able to reversibly accommodate anions. However, so far, only PTPAn has been successfully extended to Mg batteries, showing a limited specific capacity.[23] Recently, anion-involved ($AlCl_4^-$ or Cl^-) Te/Te^{4+} conversion has been demonstrated in Al batteries with the $AlCl_3$/1-ethyl-3-methylimidazolium chloride electrolyte[31] and Zn batteries with 1-butyl-3-methylimidazolium chloride/ ethylene glycol/ $ZnCl_2$ electrolyte.[32] In principle, this conversion electrochemistry holds great potential for advanced Mg//Te dual-ion batteries, given the excellent electronic conductivity of Te,[33] high theoretical specific capacity for anion storage (840 mAh g_{Te}^{-1}), and appropriate redox potential (−0.56–0.84 V vs. SHE).[32] It is evident that electrolytes play a crucial role in realizing desirable Mg//Te dual-ion batteries by providing favorable anion species without compromising the Mg stripping/plating capability. Nevertheless, the field of Mg batteries still lacks suitable electrolyte designs for such a promising dual-ion configuration, as early studies primarily focused on the dynamic behaviors of Mg^{2+}, with a limited understanding of anion behavior.

In this study, we unlock the reversible four-electron Te^0/Te^{4+} conversion in elemental Te by tailoring the classic magnesium aluminum chloride complex (MACC) electrolyte, and demonstrate superior Mg//Te dual-ion batteries (Figure 1). The Te^0/Te^{4+} conversion is initiated through the introduction of Mg bis(trifluoromethanesulfonyl)imide ($Mg(TFSI)_2$) into the MACC electrolyte (denoted MACC-TFSI), presenting two distinct charge-storage steps. Importantly, the Te electrode achieves a high specific capacity of 543 mAh g_{Te}^{-1} at 0.4 A g_{Te}^{-1} and an outstanding energy density of 850 Wh kg_{Te}^{-1}, which outperforms the majority of reported Mg^{2+}-based intercalation-type/conversion-type Mg battery cathodes and anion-involved Mg battery cathodes. With X-ray photoelectron spectroscopy (XPS) and X-ray absorption spectroscopy (XAS), we unveil that the Te cathode undergoes the Te/$TeCl_4$ conversion reaction with Cl^- as desirable charge carriers, and a tellurium subchloride phase is generated as the redox intermediate. Our assessment of MACC and MACC-TFSI electrolytes highlights that the addition of $Mg(TFSI)_2$ reduces the overall ion-molecule interaction and mitigates the strength of ion-solvent aggregation within the electrolyte. This observation indicates the facilized Cl^- dissociation from the electrolyte, especially from the $AlCl_4^-$ species, thus accounting for the initiation of Te^0/Te^{4+} conversion in MACC-TFSI. Additionally, our study verifies that $Mg(TFSI)_2$ serves as an effective buffer to mitigate the corrosion and passivation of Mg anodes caused by the consumption of the electrolyte $MgCl_2$ in Mg//Te dual-ion cells.

Results and Discussion

To trigger the Te^0/Te^{4+} conversion, we selected the classic MACC electrolyte, which comprises 0.5 M $MgCl_2$ and 0.5 M $AlCl_3$ dissolved in dimethoxyethane (DME). MACC is known to generate electro-active species, namely $MgCl^+$ and $AlCl_4^-$ in equilibrium with $MgCl_2$ and $AlCl_3$.[34] It allows favorable Mg stripping/plating with anodic stability of ~3.30 V vs. Mg/Mg^{2+} (equal to ~0.93 V vs. SHE).[35,36] However, the Te electrode fails to exhibit pronounced Te^0/Te^{4+} conversion in MACC, evidenced by the galvanostatic charge–discharge (GCD) curves measured in a two-electrode Mg//Te Swagelok cell with a glass fiber separator (Figure S1). The GCD curves show a mostly sloped shape with a limited specific capacity (< 30 mAh g^{-1}). Considering the compatible anodic stability of MACC with the Te^0/Te^{4+} conversion, we speculated that the negligible Te^0/Te^{4+} conversion was associated with the limited reaction kinetics, which could originate from the bulky and multi-atom of $AlCl_4^-$ anionic species. The direct involvement of $AlCl_4^-$ anions as charge carriers or the dissociation of Cl^- from $AlCl_4^-$ could raise a giant kinetics barrier for the Te^0/Te^{4+} conversion. In this respect, facilitating the dissociation of single-atom Cl^- from the MACC electrolyte might offer

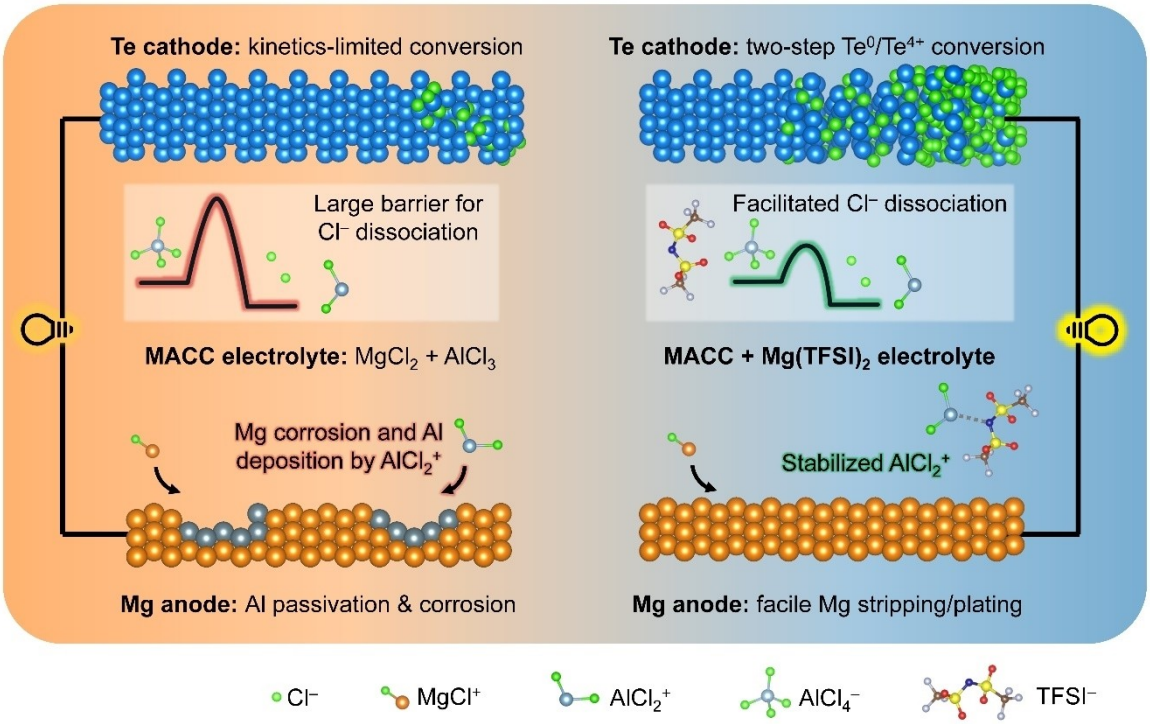

Figure 1. Schematic illustration of Mg//Te cells with the MACC electrolyte (left) and the MACC-TFSI electrolyte (right).

opportunities to realize reversible Te^0/Te^{4+} conversion with a high specific capacity and energy density.

The key to dissociating Cl^- from MACC lies in breaking the formation equilibrium of $MgCl^+$ and $AlCl_4^-$, while the capability of facile Mg stripping/plating should not be compromised. With this consideration in mind, we introduced guest anion species into MACC by adding $Mg(TFSI)_2$. Figure 2a and Figure S2 display the 2nd-cycle GCD curves of the Mg//Te cells with a voltage window of 0.4–3.1 V at 200 mA g_{Te}^{-1} in the MACC electrolytes added with different concentrations of $Mg(TFSI)_2$. Obviously, two pairs of charge/discharge plateaus at 1.0–1.4 V and 2.0–2.7 V are unlocked for the Mg//Te cell, and the specific capacity reaches a maximum (around 135 mAh g^{-1}) with a $Mg(TFSI)_2$ concentration of 0.5 M (i.e., MACC-TFSI). In addition, the Mg//Te cell with the 0.5 M $MgCl_2$ + 0.5 M $Mg(TFSI)_2$ electrolyte was also assessed. As displayed in Figure S3, the Mg//Te cell still exhibits two charge plateaus at around 1.4 and 2.8 V vs. Mg/Mg^{2+}, indicating the two-step Te^0/Te^{4+} conversion. However, the discharge curve shows only one dominant plateaus at 0.7–1.3 V vs. Mg/Mg^{2+}, reflecting a substantial charge/discharge polarization of the cell.

Notably, the addition of $Mg(TFSI)_2$ into MACC would promote the Mg stripping/plating performance,[37,38] which is evidenced by the electrochemical evaluation of MACC and MACC-TFSI. Specifically, the anode stripping/plating was assessed in an asymmetric Mg//Pt cell by the cyclic voltammetry (CV) measurements, which indicate the considerably higher current density of MACC-TFSI in comparison with MACC (Figure 2b). Furthermore, the on-set potential of Mg deposition in MACC-TFSI is determined to be −0.18 V vs. Mg/Mg^{2+}, which is only 0.05 V lower than that in MACC (Figure S4). Unlike MACC with double Mg deposition peaks, MACC-TFSI displays only a single deposition peak, which indicates the suppression of irreversible Al deposition in MACC-TFSI.[39] The GCD measurements in symmetric Mg//Mg cells further validate the desirable Mg stripping/plating kinetics of MACC-TFSI with low voltage polarization (Figure S5) and long-term cyclability (Figure 2c). At 0.1 mA cm^{-2} and 0.1 mAh cm^{-2}, MACC-TFSI allows stable Mg stripping/plating with a small polarization of 0.12 V for 200 hours. When the current density and areal capacity for the cycling test were set as 1.0 mA cm^{-2} and 1.0 mAh cm^{-2}, the Mg stripping/plating polarization slightly increased to 0.20 V (Figure S6). Besides, the anodic stability of MACC-TFSI (3.3 V vs. Mg/Mg^{2+}) is also slightly higher than that of MACC (3.2 V vs. Mg/Mg^{2+}), which was confirmed by the floating voltage test in asymmetric Mg//W cells (Figure S7).

Apparently, MACC-TFSI plays an essential role in triggering the Te conversion without the sacrifice of facile and durable Mg stripping/plating. However, the specific capacity of the Te electrode remains low compared with the theoretical value (840 mAh g_{Te}^{-1} for Te^0/Te^{4+} conversion) and also decays rapidly (10 mAh g_{Te}^{-1} after 20 cycles, Figure S8). For further improvement, we adopted a graphite oxide (GO)-coated glass fiber separator. GO has found extensive use in modifying battery separators, effectively addressing the shuttling issue common in conversion-type cathodes.[4,40] The polarized functional groups densely present on the GO surface are expect to adsorb soluble Te-species,[31] mitigating rapid capacity decay resulting from

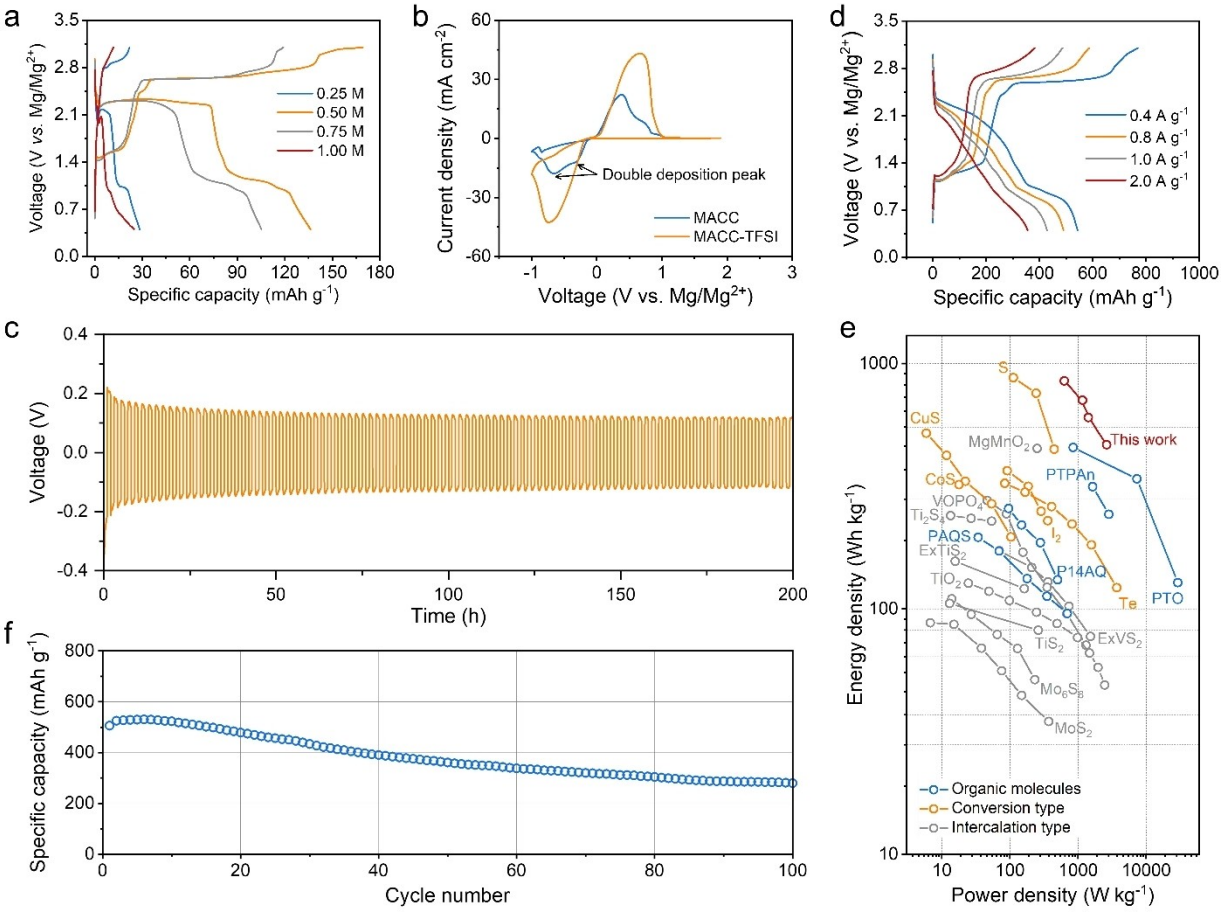

Figure 2. Electrochemical performance of the Mg//Te dual-ion battery. a) GCD curves of Mg//Te cells in the MACC electrolytes added with different concentrations of $Mg(TFSI)_2$. Pristine glass fiber separators were used. b) CV curves obtained from Mg//Pt cells using the MACC and MACC-TFSI electrolytes at a scan rate of 25 $mV\,s^{-1}$. c) Galvanostatic Mg stripping/plating in Mg//Mg symmetric cells with the MACC-TFSI electrolyte at 0.1 $mA\,cm^{-2}$ and 0.1 $mAh\,cm^{-2}$. d) GCD curves of the Mg//Te cell with the MACC-TFSI electrolyte at various current densities. A GO-covered glass fiber separator was used. e) Ragone plots presenting the energy density and power density of the Te electrode in comparison with recently reported Mg battery cathodes. All the calculations are based on the mass of active cathode materials. f) Cycling performance of the Mg//Te cell using the MACC-TFSI electrolyte at 2.0 $A\,g_{Te}^{-1}$.

active material loss. As expected, the Mg//Te cell with the MACC-TFSI electrolyte after several-cycle activation achieves a high discharge capacity of 543 $mAh\,g_{Te}^{-1}$ at a current density of 0.4 $A\,g_{Te}^{-1}$ (Figure 2d). Moreover, a high specific capacity of 356 $mAh\,g_{Te}^{-1}$ was maintained when the current density reaches 2.0 $A\,g_{Te}^{-1}$. The effective role of the GO-coated separator in inhibiting the loss of active Te-species was verified by the scanning electron microscopy (SEM) images of the Te electrode after 10 charge/discharge cycles (Figure S9). By contrast, the GO-coated separator does not improve the performance of the Mg//Te cell with the MACC electrolyte (Figure S10). This result supports that the high specific capacity of the Mg//Te cell with the MACC-TFSI electrolyte is mainly attributed to the facilitated Te^0/Te^{4+} conversion, instead of the GO-coated separator.

Based on the discharge curve of the Mg//Te cell with the MACC-TFSI electrolyte, the energy density and power density of the Te electrode are derived and compared with the recently reported cathode materials for Mg batteries (Figure 2e and Table S1). Significantly, the Te electrode achieves a maximum energy density of 850 $Wh\,kg_{Te}^{-1}$, which is comparable with the reported 'holy-grail' conversion-type S cathode with Mg^{2+} charge carriers (876 $Wh\,kg_S^{-1}$).[16] It's worth emphasizing that the Te electrode achieves its maximum energy density at a power density of 630 $W\,kg_{Te}^{-1}$, which is 5.6 times higher than the reported power density for the S cathode (112 $W\,kg_S^{-1}$). This desirable high-power feature of the Te electrode could be attributed to the involvement of anion charge carriers, which promotes the conversion kinetics compared with Mg^{2+} as charge carriers. Besides, the energy density of the Te electrode substantially surpasses the recently reported intercalation-type (e.g., 451 $Wh\,kg^{-1}$ for $MgMnO_2$,[8] 277 $Wh\,kg^{-1}$ for $VOPO_4$,[41] 240 $Wh\,kg^{-1}$ for Ti_2S_4,[12] 173 $Wh\,kg^{-1}$ for expanded VS_2 ($ExVS_2$),[42] 156 $Wh\,kg^{-1}$ for expanded TiS_2 ($ExTiS_2$),[20] 127 $Wh\,kg^{-1}$ for TiO_2,[43] 110 $Wh\,kg^{-1}$ for Mo_6S_8,[11] and 88 $Wh\,kg^{-1}$ for MoS_2).[22] conversion-type (e.g., 366 $Wh\,kg^{-1}$ for iodine,[44] 321 $Wh\,kg^{-1}$ for CoS,[13] and 520 $Wh\,kg^{-1}$ for CuS),[14] organic cathode (such as 455 $Wh\,kg^{-1}$ for PTO,[4]

196 Wh kg^{-1} for PAQS,[17] and 257 Wh kg^{-1} for P14AQ[18] and anion-storage cathodes (e.g., 315 Wh kg^{-1} for PTPAn).[23] Additionally, with the GO-coated separator, the Te electrode exhibits decent cyclability compared to the typical conversion-type electrodes (Figure 2f). After 100 charge/discharge cycles at 2.0 A g_{Te}^{-1}, the Te electrode can maintain a specific capacity of 280 mAh g_{Te}^{-1}. Moreover, a specific capacity of 308 mAh g_{Te}^{-1} was retained after 100 GCD cycles at 1.0 A g_{Te}^{-1} (Figure S11). The observed decline in cycling capacity could result from several factors, such as incomplete inhibition of Te-species dissolution, structural collapse accelerated by the significant volume change during the conversion reaction, and anode passivation caused by the dissolved Te-species. Further improvement in cyclability could be anticipated by exploring advanced Te-based hybrids and constructing a suitable electrode/electrolyte interphase to confine active Te species, which warrants further exploration in future research.

To elucidate the conversion mechanism of Te in MACC-TFSI, XPS was conducted to monitor the chemical states of Te at different charge states. At the fully discharged state (0.4 V vs. Mg/Mg^{2+}), the Te 3d XPS spectrum exhibited two sharp peaks at 583.7 eV and 573.3 eV (Figure 3a), corresponding to the characteristic $3d_{3/2}$ and $3d_{5/2}$ peaks of Te^0, respectively.[31,32] These peaks aligned with the Te 3d XPS peaks detected in the initial Te electrode (Figure S12), confirming elemental Te as the final discharge product. Importantly, no Te^{2-} species were observed in the fully discharged electrode,[45] which can be attributed to the sluggish kinetics of the Mg^{2+}-involved conversion, including large dissociation energy barriers and slow solid-state diffusivity of Mg^{2+}.[45] Upon charging the Te electrode to 1.5 V vs. Mg/Mg^{2+}, an intermediate state between the two charge plateaus of Te, characteristic $3d_{3/2}$ and $3d_{5/2}$ peaks of Te^{2+} at 585.8 eV and 574.5 eV were detected. These two peaks imply the formation of metastable tellurium subchlorides, in which partial Te atoms in the Te chain bind with two chlorine atoms axially, like the Te_3Cl_2 structure.[46] Additional Te^{4+} peaks at 587.7 eV and 577.3 eV were also observed, which could come from the oxidation of active Te^{2+} species once exposed to air.[32] Further charging the Te electrode to 3.1 V vs. Mg/Mg^{2+} led to a significant increase in the intensity of Te^{4+} peaks. These XPS results signify that the Te^0/Te^{4+} conversion serves as the dominant Faradaic reaction, enabling the high specific capacity of the Te electrode.

Additionally, the Te^0/Te^{4+} conversion is supported by the X-ray absorption near-edge structure (XANES) analysis of the Te electrodes in comparison with standard references (i.e., Te, TeO_2, $TeCl_4$, and ZnTe). As shown in Figure 3b, the discharged Te electrode shows almost the identical Te K-edge spectrum shape with standard Te reference. The absence of Te^{2-} in the discharged electrode was evidenced by the fact that Te^{2-} (ZnTe reference) has considerably higher edge energy than Te^0 (Te reference, Figure 3c). Along with charging to 3.1 V vs. Mg/Mg^{2+}, the Te K-edge XANES shows a gradually increased edge peak at 31,800 eV (Figure 3b), which agrees well with the spectrum evolution trend from Te^0 (Te reference) to Te^{4+} ($TeCl_4$ and TeO_2 references) shown in Figure 3c.

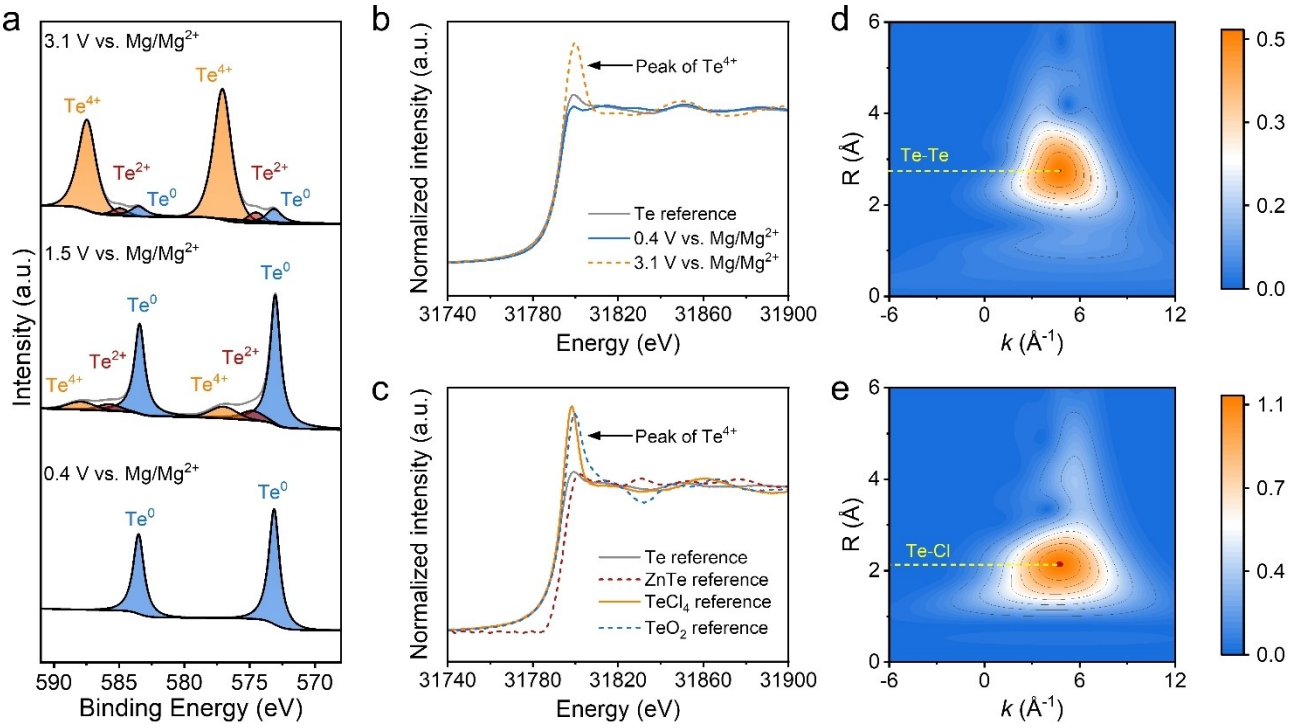

Figure 3. Te cathode charge species. a) Te 3d core level XPS spectra of the Te electrode at 0.4 V, 1.5 V, and 3.1 V vs. Mg/Mg^{2+}. b) Te K-edge XANES spectra of the Te electrode at 0.4 V and 3.1 V vs. Mg/Mg^{2+} in comparison with Te reference. c) Te K-edge XANES spectra of Te, ZnTe, $TeCl_4$ and TeO_2 references. Wavelet-transformed Te K-edge EXAFS of the Te electrode at d) 0.4 V and e) 3.1 V vs. Mg/Mg^{2+}.

To further elucidate the fully charged and discharged products, we probed into the local coordination environment of Te with extended X-ray absorption fine structure (EXAFS). The wavelet transform (WT) analysis on the k^2-weighted EXAFS data with a 2D representation in R and k spaces was conducted for the fully discharged and charged Te electrodes, as well as standard references. Specifically, the fully discharged Te electrode exhibits the WT maxima position at R = 2.75 Å (Figure 3d), which refers to the Te–Te scattering as observed in Te reference (Figure S13). Moreover, the EXAFS result of the fully discharged Te electrode can be well fitted with only Te–Te path (as in elemental Te, space group: $P3_121$) with a coordination number (N) of 2 (Figure S14 and Table S2). Meanwhile, the dominant WT maxima position of the fully charged Te electrode appears at R = 2.15 Å (Figure 3e), which aligns with the Te–Cl path from $TeCl_4$ reference (Figure S13). Accordingly, the EXAFS spectrum of the fully charged Te electrode was well fitted with three coordination paths (Figure S14 and Table S3), including Te–Te as in elemental Te, Te–O as in crystalline TeO_2 (space group: $P2_12_12_1$), and Te–Cl as in crystalline $TeCl_4$ (space group: $C2/c$). The presence of Te–Te and Te–O could be attributed to the unconverted Te and inevitable hydrolysis of $TeCl_4$ upon exposure to air, respectively.

All the above analyses manifest a two-step Te^0/Te^{4+} conversion mechanism, where elemental Te and $TeCl_4$ serve as the discharge and charge products, respectively. The intermediate state is estimated to be a tellurium subchloride like Te_3Cl_2, the only acknowledged metastable phase of tellurium chloride aside from $TeCl_4$. This two-step conversion mechanism was also verified by the calculated Gibbs free energy (Figure S15), in which a potential gap of 1.0 V was observed between the Te/Te_3Cl_2 conversion and the $Te_3Cl_2/TeCl_4$ conversion. This potential gap agrees well with that of the two plateaus in the GCD curves of the Te electrode. Therefore, the anode, cathode, and the overall reactions of the Mg//Te cell can be described as equation (1–3).

$$\textbf{Anode reaction}: \ Mg^{2+} + 2\,e^- \leftrightarrow Mg \quad (1)$$

$$\textbf{Cathode reaction}: \ Te + 4\,Cl^- \leftrightarrow TeCl_4 + 4\,e^- \quad (2)$$

$$\textbf{Overall reaction}: \ Te + 2\,MgCl_2 \leftrightarrow 2Mg + TeCl_4 \quad (3)$$

Apparently, Cl^- anion dynamics in the electrolyte plays a pivotal role in triggering the reversible $Te/TeCl_4$ conversion. We first carried out wide-/small-angle X-ray scattering (WAXS/SAXS) measurements to understand the micro species in the MACC and MACC-TFSI electrolytes. In the WAXS result (Figure 4a), the scattering vector (q) ranges from 6 to 30 nm^{-1}, which covers the characteristic distance (d) from 10.5 to 1.05 Å based on equation (4). The peak at $q = 15.4\ nm^{-1}$ of both MACC and MACC-TFSI comes from free solvent molecules (i.e., DME), which can be confirmed by the spectrum of pure DME. The peak refers to a characteristic intermolecular distance of 4.1 Å for DME.[47] In MACC, the addition of salts triggers the distribution of molecules by forming solvated anion/cations and ion pairs.[48] Thereby, an additional peak at $q = 10.9\ nm^{-1}$ was detected, corresponding to the intermolecular distance (5.7 Å) of

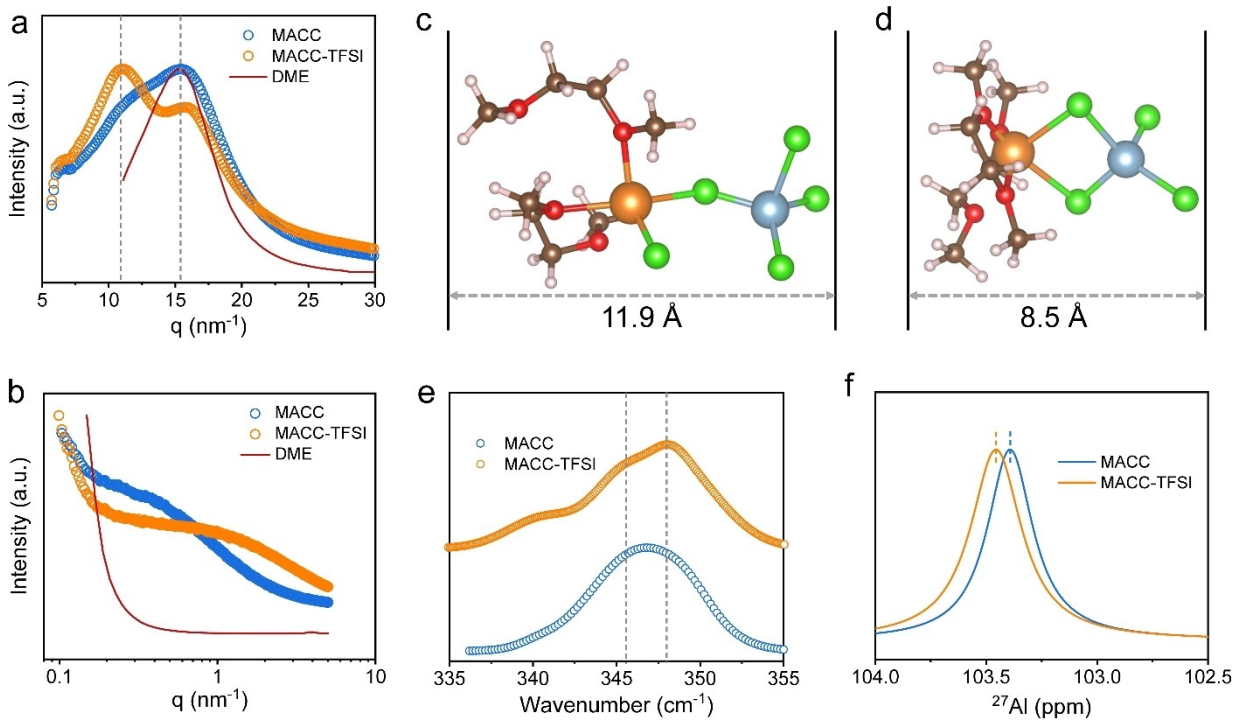

Figure 4. Electrolyte characterizations. a) WAXS and b) SAXS profiles of MACC and MACC-TFSI. Representative $AlCl_4^-$-containing clusters in c) MACC and d) MACC-TFSI derived from the snapshots through AIMD simulations. e) Raman and f) ^{27}Al NMR spectra of MACC and MACC-TFSI.

these solvated species. After the addition of $Mg(TFSI)_2$, a noticeable increase in intensity is observed for the peak at $q = 10.9\ nm^{-1}$, accompanied by a decrease in intensity of the peak at $q = 15.4\ nm^{-1}$. This finding signifies an increase in solvated species and a reduction in free solvents within MACC-TFSI when compared with MACC. Meanwhile, SAXS spectra with q ranging from 0.1 to 5 nm^{-1} indicate the intramolecular scattering with the characteristic distance from 62.8 nm to 12.5 Å (Figure 4b). In $0.3 < q < 5\ nm^{-1}$, pure DME shows a flat plateau, manifesting the random distribution of molecules in the liquid. By contrast, dramatic uplift was observed for MACC and MACC-TFSI in this q range, corresponding to the formation of large-size ion-solvent aggregates. In comparison with MACC, MACC-TFSI shows a signal shift towards higher q values with a lower scattering distance. This finding indicates that the addition of $Mg(TFSI)_2$ could weaken the overall ion-molecule interaction and mitigate the ion-solvent aggregation strength. According to the classic Stokes–Einstein equation, which describes an inverse relationship between the diffusion coefficient and particle radius, small ion-solvent aggregates could benefit the fast transport and dissociation of Cl^- from the electrolyte.[49–51]

$$d = 2\pi/q \tag{4}$$

Next, we put our emphasis on analyzing the $AlCl_4^-$ species in MACC and MACC-TFSI, as it is the main anion species in the two electrolytes. Using ab initio molecular dynamics (AIMD) simulations (Figure S16), we derived the representative clusters that contain $AlCl_4^-$ in MACC (Figure 4c) and in MACC-TFSI (Figure 4d). $AlCl_4^-$ of MACC-TFSI is involved in a smaller ion-solvent aggregate in comparison with $AlCl_4^-$ in MACC, which agrees with the indication from the SAXS analysis. Furthermore, we collected Raman spectra of MACC and MACC-TFSI (Figure S17). Figure 4e zooms into the characteristic $AlCl_4^-$ peak at ca. 346.8 cm^{-1} (A_1 symmetric stretching). It is found that the $AlCl_4^-$ peak of MACC-TFSI splits into two shoulder peaks due to its surrounding interaction change by the addition of $Mg(TFSI)_2$. Besides, ^{27}Al NMR spectra (Figure 4f and Figure S18) manifest a downfield shift of the characteristic $AlCl_4^-$ peak in MACC-TFSI (103.5 ppm) compared with the $AlCl_4^-$ peak in MACC (103.4 ppm). This observation indicates that the electron density decreases around the Al atom in $AlCl_4^-$ in MACC-TFSI,[52,53] which points to the promoted Cl^- dissociation from $AlCl_4^-$ in MACC-TFSI.

We further probed into the Mg anode of Mg//Te cells to understand the effect of Te^0/Te^{4+} conversion on the Mg anode, considering the consumption of $MgCl_2$ salt in the electrolyte during battery charging (equation (3)). Both Mg//Te cells with MACC and MACC-TFSI were cycled for 10 charge/discharge cycles at 200 mA g_{Te}^{-1}, and their Mg anodes were subjected to the SEM and energy-dispersive X-ray (EDX) spectroscopy analyses. Notably, the Mg anode in MACC shows an aggressive corrosion issue with a large number of voids visualized on the surface (Figure 5a). Surface passivation by irreversible Al deposition appears as another critical concern, which can be identified by EDX elemental mapping (Figure 5b). The quantified Al/Mg atomic ratio reaches 10 % on the Mg anode surface (Figure S19). Moreover, compared with Mg electrode of Mg//Mg symmetric cell after 10 stripping/plating cycles at 0.1 mA g^{-1} and 0.1 mAh g^{-1} (Figure S20), both corrosion and Al passivation issues become more serious. We should also

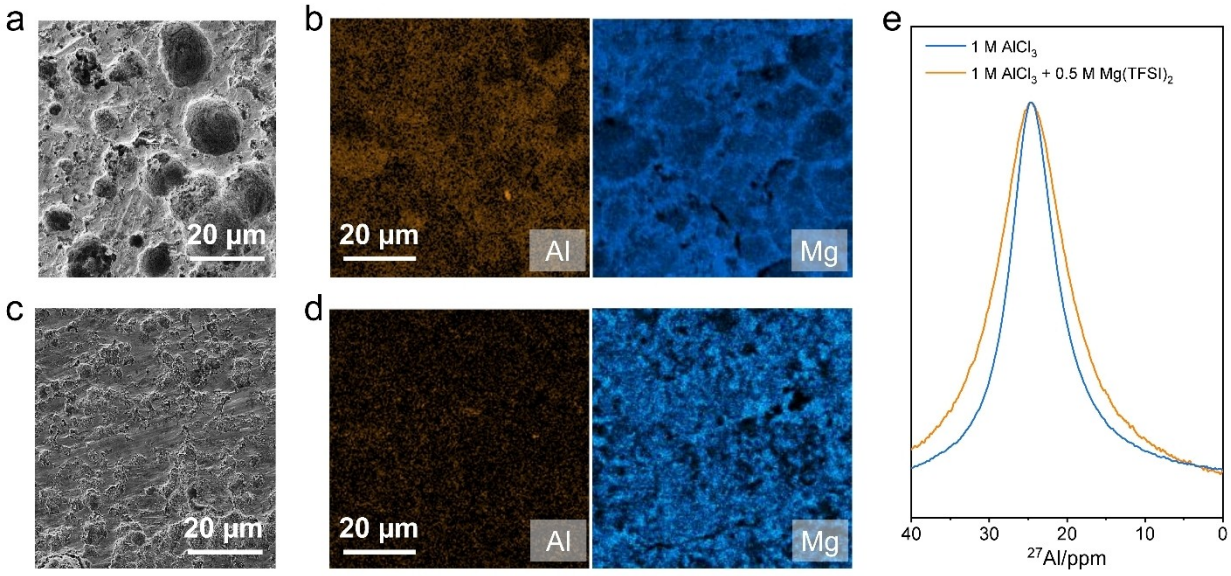

Figure 5. Analysis of Mg anode in Mg//Te dual-ion cell. a) SEM image and b) EDX elemental mapping (Al, Mg) of the Mg anode surface from Mg//Te cell with MACC electrolyte after 10 charge/discharge cycles at 200 mA g_{Te}^{-1}. c) SEM image and d) EDX elemental mapping (Al, Mg) of the Mg anode surface from Mg//Te cell with MACC-TFSI electrolyte after 10 charge/discharge cycles at 200 mA g_{Te}^{-1}. e) ^{27}Al NMR spectra of 1 M $AlCl_3$ in diglyme and 1 M $AlCl_3$ + 0.5 M $Mg(TFSI)_2$ in diglyme.

mention that the accelerated effects cannot be simply associated with the side electrolyte decomposition on the Te cathode, which can be evidenced by a control floating test in the Mg//W cell (Figure S21). Instead, the Te^0/Te^{4+} conversion accelerated the side effects of Mg anode in MACC due to the consumption of $MgCl_2$ in the electrolyte during cell charging. The $MgCl_2$ consumption breaks the equilibrium of equation (5), leading to the presence of excessive Lewis-acidic $AlCl_3$ and enhanced corrosive ability of MACC.[39,54] Besides, the excessive $AlCl_3$ could generate active $AlCl_2^+$ through equation (6) and intensify the Al passivation.[55,56]

$$AlCl_3 + MgCl_2 \leftrightarrow AlCl_4^- + MgCl^+ \quad (5)$$

$$2AlCl_3 \leftrightarrow AlCl_4^- + AlCl_2^+ \quad (6)$$

Compared with MACC, MACC-TFSI can substantially mitigate the corrosion and passivation issue on the Mg anode in Mg//Te cell. The surface of the Mg anode after 10 cycles at 200 mA g^{-1} appears relatively flat and homogeneous (Figure 5c), while the Al/Mg atomic ratio is only 4 % (Figure 5d and Figure S22). To understand the effect of the added $Mg(TFSI)_2$ on stabilizing the excessive $AlCl_3$, we prepared two control electrolytes, namely 1 M $AlCl_3$ in diglyme and 1 M $AlCl_3$ + 0.5 M $Mg(TFSI)_2$ in diglyme. Figure 5e and Figure S23 compare the characteristic ^{27}Al NMR signal at 24.8 ppm for $AlCl_2^+$ in both electrolytes.[56] Compared with 1 M $AlCl_3$, the $Mg(TFSI)_2$ addition causes apparent signal broadening as observed for $AlCl_2(amide)_2$ species,[57] which implies the formation of $AlCl_2^+$-$TFSI^-$ aggregates in 1 M $AlCl_3$ + 0.5 M $Mg(TFSI)_2$. These findings suggest the buffer effect of $Mg(TFSI)_2$ on stabilizing the excessive $AlCl_3$ in MACC-TFSI, particularly the formed active $AlCl_2^+$ species, thereby effectively mitigating the corrosion and Al passivation of Mg anode.

Conclusion

In summary, we have demonstrated a novel Mg//Te dual-ion battery by unlocking the reversible four-electron Te^0/Te^{4+} conversion in elemental Te. This was achieved by tailoring the classic MACC electrolyte with $Mg(TFSI)_2$ to initiate the two-step conversion of Te. Importantly, the Te electrode achieved a high specific capacity of 543 mAh g_{Te}^{-1} and an outstanding energy density of 850 Wh kg_{Te}^{-1}, outperforming the majority of reported Mg^{2+}-based intercalation-type and conversion-type cathodes, as well as anion-involved cathodes for Mg-based batteries. It was revealed that the Te cathode underwent the $Te/TeCl_4$ conversion reaction with Cl^- as charge carriers, and a tellurium subchloride phase was generated as a redox intermediate. Furthermore, the analysis of MACC and MACC-TFSI indicated that the addition of $Mg(TFSI)_2$ reduced the overall ion-molecule interaction and weakened the strength of ion-solvent aggregation. These changes could promote the Cl^- dissociation from the electrolyte species, particularly from $AlCl_4^-$, accounting for the initiation of Te^0/Te^{4+} conversion in MACC-TFSI. Moreover, $Mg(TFSI)_2$ in MACC-TFSI was revealed as an effective electrolyte buffer to mitigate the corrosion and passivation of Mg anodes caused by the consumption of the electrolyte $MgCl_2$ in Mg//Te dual-ion cells. All these findings provide immense insights into the development of high-performance magnesium-based dual-ion batteries.

Supporting Information

Supporting Information is available from the Wiley Online Library.

Acknowledgements

This work was financially supported by European Union's Horizon Europe research and innovation programme (ERC Starting Grant, BattSkin, 101116722), European Union's Horizon 2020 research and innovation programme (LIGHTCAP 101017821), German Research Foundation (DFG) within the Cluster of Excellence, CRC 1415 (Grant No. 417590517), and the European Fonds for Regional Development (Europäischer Fonds für Regionale Entwicklung; EFRE-OP 2014–2020; Project No. 2021 FGI 0035, NanoLabXPS) as part of the REACT-EU program. The authors also acknowledge the use of the facilities in the Dresden Center for Nanoanalysis (DCN) at Technische Universität Dresden, the GWK support for providing computing time through the Center for Information Services and High-Performance Computing (ZIH) at TU Dresden. We acknowledge DESY (Hamburg, Germany), a member of the Helmholtz Association HGF, for the provision of experimental facilities. Parts of this research were carried out at PETRA III, and we would like to thank Edmund Welter and Dr. Andre L. C Conceição for assistance in using beamlines P65 and P62, respectively. WAXS experiments were also performed at BL11 beamline at ALBA Synchrotron with the collaboration of Dr. Cristián Huck Iriart. We acknowledge the European Synchrotron Radiation Facility (ESRF) for the provision of synchrotron radiation facilities, and we would like to thank Dr. Cesare Atzorifor's assistance and support in using beamline BM23. We also thank Mr. Lukas Sporrer for helping with material characterization. Open Access funding enabled and organized by Projekt DEAL.

Conflict of Interest

The authors declare no conflict of interest.

Data Availability Statement

The data that support the findings of this study are available from the corresponding author upon reasonable request.

Keywords: magnesium batteries · dual-ion batteries · conversion-type cathodes · anion charge carriers · tellurium

[1] Y. Liang, H. Dong, D. Aurbach, Y. Yao, *Nat. Energy* **2020**, *5*, 646–656.
[2] Y. Tian, G. Zeng, A. Rutt, T. Shi, H. Kim, J. Wang, J. Koettgen, Y. Sun, B. Ouyang, T. Chen, Z. Lun, Z. Rong, K. Persson, G. Ceder, *Chem. Rev.* **2021**, *121*, 1623–1669.
[3] G. Wang, M. Yu, X. Feng, *Chem. Soc. Rev.* **2021**, *50*, 2388–2443.
[4] H. Dong, O. Tutusaus, Y. Liang, Y. Zhang, Z. Lebens-Higgins, W. Yang, R. Mohtadi, Y. Yao, *Nat. Energy* **2020**, *5*, 1043–1050.
[5] J. Luo, Y. Bi, L. Zhang, X. Zhang, T. L. Liu, *Angew. Chem. Int. Ed.* **2019**, *58*, 6967–6971.
[6] W. Zhao, Z. Pan, Y. Zhang, Y. Liu, H. Dou, Y. Shi, Z. Zuo, B. Zhang, J. Chen, X. Zhao, X. Yang, *Angew. Chem. Int. Ed.* **2022**, *61*, e202205187.
[7] A. Morag, X. Chu, C. Neumann, D. Pohl, M. Borrelli, D. Sabaghi, M. Löffler, Z. Sofer, A. Turchanin, M. Yu, X. Feng, *Energy Storage Mater.* **2022**, *53*, 435–443.
[8] S. Hou, X. Ji, K. Gaskell, P. Wang, L. Wang, J. Xu, R. Sun, O. Borodin, C. Wang, *Science (1979)* **2021**, *374*, 172–178.
[9] M. Mao, Z. Lin, Y. Tong, J. Yue, C. Zhao, J. Lu, Q. Zhang, L. Gu, L. Suo, Y.-S. Hu, H. Li, X. Huang, L. Chen, *ACS Nano* **2020**, *14*, 1102–1110.
[10] D. Aurbach, Z. Lu, A. Schechter, Y. Gofer, H. Gizbar, R. Turgeman, Y. Cohen, M. Moshkovich, E. Levi, *Nature* **2000**, *407*, 724–727.
[11] C. Liao, B. Guo, D. Jiang, R. Custelcean, S. M. Mahurin, X.-G. Sun, S. Dai, *J. Mater. Chem. A* **2014**, *2*, 581–584.
[12] X. Sun, P. Bonnick, V. Duffort, M. Liu, Z. Rong, K. A. Persson, G. Ceder, L. F. Nazar, *Energy Environ. Sci.* **2016**, *9*, 2273–2277.
[13] M. Pan, J. Zou, R. Laine, D. Khan, R. Guo, X. Zeng, W. Ding, *J. Mater. Chem. A* **2019**, *7*, 18880–18888.
[14] M. Mao, T. Gao, S. Hou, F. Wang, J. Chen, Z. Wei, X. Fan, X. Ji, J. Ma, C. Wang, *Nano Lett.* **2019**, *19*, 6665–6672.
[15] Z. Zhang, Z. Cui, L. Qiao, J. Guan, H. Xu, X. Wang, P. Hu, H. Du, S. Li, X. Zhou, S. Dong, Z. Liu, G. Cui, L. Chen, *Adv. Energy Mater.* **2017**, *7*, 1602055.
[16] A. Du, Z. Zhang, H. Qu, Z. Cui, L. Qiao, L. Wang, J. Chai, T. Lu, S. Dong, T. Dong, H. Xu, X. Zhou, G. Cui, *Energy Environ. Sci.* **2017**, *10*, 2616–2625.
[17] B. Pan, J. Huang, Z. Feng, L. Zeng, M. He, L. Zhang, J. T. Vaughey, M. J. Bedzyk, P. Fenter, Z. Zhang, A. K. Burrell, C. Liao, *Adv. Energy Mater.* **2016**, *6*, 1600140.
[18] H. Dong, Y. Liang, O. Tutusaus, R. Mohtadi, Y. Zhang, F. Hao, Y. Yao, *Joule* **2019**, *3*, 782–793.
[19] A. Morag, M. Yu, *J. Mater. Chem. A* **2021**, *9*, 19317–19345.
[20] H. D. Yoo, Y. Liang, H. Dong, J. Lin, H. Wang, Y. Liu, L. Ma, T. Wu, Y. Li, Q. Ru, Y. Jing, Q. An, W. Zhou, J. Guo, J. Lu, S. T. Pantelides, X. Qian, Y. Yao, *Nat. Commun.* **2017**, *8*, 339.
[21] J. Muldoon, C. B. Bucur, T. Gregory, *Angew. Chem. Int. Ed.* **2017**, *56*, 12064–12084.
[22] Z. Li, X. Mu, Z. Zhao-Karger, T. Diemant, R. J. Behm, C. Kübel, M. Fichtner, *Nat. Commun.* **2018**, *9*, 5115.
[23] Y. Xiu, A. Mauri, S. Dinda, Y. Pramudya, Z. Ding, T. Diemant, A. Sarkar, L. Wang, Z. Li, W. Wenzel, M. Fichtner, Z. Zhao-Karger, *Angew. Chem. Int. Ed.* **2023**, *62*, e202212339.
[24] M. Wang, C. Jiang, S. Zhang, X. Song, Y. Tang, H.-M. Cheng, *Nat. Chem.* **2018**, *10*, 667–672.
[25] G. Wang, B. Kohn, U. Scheler, F. Wang, S. Oswald, M. Löffler, D. Tan, P. Zhang, J. Zhang, X. Feng, *Adv. Mater.* **2020**, *32*, e1905681.
[26] Y. Liu, Y. Lu, A. Hossain Khan, G. Wang, Y. Wang, A. Morag, Z. Wang, G. Chen, S. Huang, N. Chandrasekhar, D. Sabaghi, D. Li, P. Zhang, D. Ma, E. Brunner, M. Yu, X. Feng, *Angew. Chem. Int. Ed.* **2023**, *62*, e202306091.
[27] G. Wang, E. Dmitrieva, B. Kohn, U. Scheler, Y. Liu, V. Tkachova, L. Yang, Y. Fu, J. Ma, P. Zhang, F. Wang, J. Ge, X. Feng, *Angew. Chem. Int. Ed.* **2022**, *61*, e202116194.
[28] M. C. Lin, M. Gong, B. Lu, Y. Wu, D. Y. Wang, M. Guan, M. Angell, C. Chen, J. Yang, B. J. Hwang, H. Dai, *Nature* **2015**, *520*, 324–328.
[29] C. N. Gannett, B. M. Peterson, L. Shen, J. Seok, B. P. Fors, H. D. Abruña, *ChemSusChem* **2020**, *13*, 2428–2435.
[30] M. Kato, K. I. Senoo, M. Yao, Y. Misaki, *J. Mater. Chem. A* **2014**, *2*, 6747–6754.
[31] X. Zhang, S. Jiao, J. Tu, W.-L. Song, X. Xiao, S. Li, M. Wang, H. Lei, D. Tian, H. Chen, D. Fang, *Energy Environ. Sci.* **2019**, *12*, 1918–1927.
[32] Z. Chen, S. Wang, Z. Wei, Y. Wang, Z. Wu, Y. Hou, J. Zhu, Y. Wang, G. Liang, Z. Huang, A. Chen, D. Wang, C. Zhi, *J. Am. Chem. Soc.* **2023**, *145*, 20521–20529.
[33] J. Zhang, Y.-X. Yin, Y.-G. Guo, *ACS Appl. Mater. Interfaces* **2015**, *7*, 27838–27844.
[34] P. Canepa, S. Jayaraman, L. Cheng, N. N. Rajput, W. D. Richards, G. S. Gautam, L. A. Curtiss, K. A. Persson, G. Ceder, *Energy Environ. Sci.* **2015**, *8*, 3718–3730.
[35] J. Luo, S. He, T. L. Liu, *ACS Energy Lett.* **2017**, *2*, 1197–1202.
[36] Y. Li, S. Guan, H. Huo, Y. Ma, Y. Gao, P. Zuo, G. Yin, *Adv. Funct. Mater.* **2021**, *31*, 2100650.
[37] L. Yang, C. Yang, Y. Chen, Z. Pu, Z. Zhang, Y. Jie, X. Zheng, Y. Xiao, S. Jiao, Q. Li, D. Xu, *ACS Appl. Mater. Interfaces* **2021**, *13*, 30712–30721.
[38] Y. He, Q. Li, L. Yang, C. Yang, D. Xu, *Angew. Chem. Int. Ed.* **2019**, *58*, 7615–7619.
[39] C. J. Barile, E. C. Barile, K. R. Zavadil, R. G. Nuzzo, A. A. Gewirth, *J. Phys. Chem. C* **2014**, *118*, 27623–27630.
[40] J.-Q. Huang, T.-Z. Zhuang, Q. Zhang, H.-J. Peng, C.-M. Chen, F. Wei, *ACS Nano* **2015**, *9*, 3002–3011.
[41] L. Zhou, Q. Liu, Z. Zhang, K. Zhang, F. Xiong, S. Tan, Q. An, Y.-M. Kang, Z. Zhou, L. Mai, *Adv. Mater.* **2018**, *30*, e1801984.
[42] X. Xue, R. Chen, C. Yan, P. Zhao, Y. Hu, W. Kong, H. Lin, L. Wang, Z. Jin, *Adv. Energy Mater.* **2019**, *9*, 1900145.
[43] J. Yang, J. Li, W. Gong, F. Geng, *PNAS* **2021**, *118*, e2111549118.
[44] H. Tian, T. Gao, X. Li, X. Wang, C. Luo, X. Fan, C. Yang, L. Suo, Z. Ma, W. Han, C. Wang, *Nat. Commun.* **2017**, *8*, 14083.
[45] Z. Chen, Q. Yang, D. Wang, A. Chen, X. Li, Z. Huang, G. Liang, Y. Wang, C. Zhi, *ACS Nano* **2022**, *16*, 5349–5357.
[46] J. Haag, U. V. Alpen, E. Gmelin, A. Rabenau, *Z. Naturforsch. A* **1979**, *34*, 969–975.
[47] K. Shimizu, A. A. Freitas, R. Atkin, G. G. Warr, P. A. FitzGerald, H. Doi, S. Saito, K. Ueno, Y. Umebayashi, M. Watanabe, J. N. Canongia Lopes, *Phys. Chem. Chem. Phys.* **2015**, *17*, 22321–22335.
[48] K. Qian, Z. Yu, Y. Liu, D. J. Gosztola, R. E. Winans, L. Cheng, T. Li, *J. Energy Chem.* **2022**, *70*, 340–346.
[49] K. Qian, R. E. Winans, T. Li, *Adv. Energy Mater.* **2021**, *11*, 2002821.
[50] S. Saito, H. Watanabe, K. Ueno, T. Mandai, S. Seki, S. Tsuzuki, Y. Kameda, K. Dokko, M. Watanabe, Y. Umebayashi, *J. Phys. Chem. B* **2016**, *120*, 3378–3387.
[51] S. C. Kim, J. Wang, R. Xu, P. Zhang, Y. Chen, Z. Huang, Y. Yang, Z. Yu, S. T. Oyakhire, W. Zhang, L. C. Greenburg, M. S. Kim, D. T. Boyle, P. Sayavong, Y. Ye, J. Qin, Z. Bao, Y. Cui, *Nat. Energy* **2023**, *8*, 814–826.
[52] H. Xu, T. Bai, H. Chen, F. Guo, J. Xi, T. Huang, S. Cai, X. Chu, J. Ling, W. Gao, Z. Xu, C. Gao, *Energy Storage Mater.* **2019**, *17*, 38–45.
[53] D. Paterno, E. Rock, A. Forbes, R. Iqbal, N. Mohammad, S. Suarez, *J. Mol. Liq.* **2020**, *319*, 114118.

[54] G. Bieker, M. Salama, M. Kolek, Y. Gofer, P. Bieker, D. Aurbach, M. Winter, *ACS Appl. Mater. Interfaces* **2019**, *11*, 24057–24066.
[55] A. Kitada, K. Nakamura, K. Fukami, K. Murase, *Electrochim. Acta* **2016**, *211*, 561–567.
[56] Z. Zhang, A. Kitada, S. Gao, K. Fukami, N. Tsuji, Z. Yao, K. Murase, *ACS Appl. Mater. Interfaces* **2020**, *12*, 43289–43298.
[57] W. Chu, X. Zhang, J. Wang, S. Zhao, S. Liu, H. Yu, *Energy Storage Mater.* **2019**, *22*, 418–423.

Manuscript received: January 25, 2024
Accepted manuscript online: March 11, 2024
Version of record online: ■■, ■■

Research Articles

Mg Dual-ion Batteries

A. Morag, X. Chu, M. Marczewski, J. Kunigkeit, C. Neumann, D. Sabaghi, G. Z. Żukowska, J. Du, X. Li, A. Turchanin, E. Brunner, X. Feng,* M. Yu* e202401818

Unlocking Four-electron Conversion in Tellurium Cathodes for Advanced Magnesium-based Dual-ion Batteries

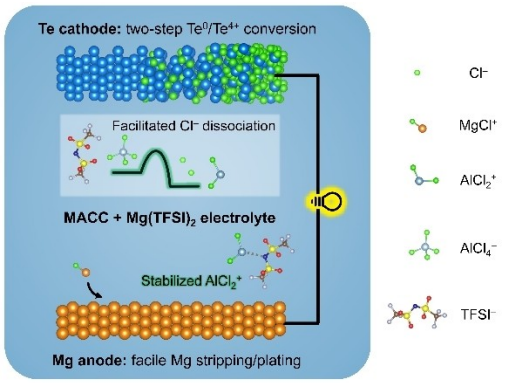

Mg//Te dual-ion battery

In a magnesium aluminum chloride complex electrolyte with $Mg(TFSI)_2$ additive, a four-electron Te^0/Te^{4+} conversion is initiated in elemental Te, enabling the demonstration of high-performance Mg//Te dual-ion batteries. The $Mg(TFSI)_2$ additive is uncovered to play a crucial role in facilitating Cl^- dissociation and mitigating corrosion and passivation of Mg anodes.